International Journal of
Geo-Information

IMPACT FACTOR 3.2

CITESCORE 6.7

Article

Spatial Methods for Identifying Undocumented Historical Earthquake Damage

Adi Ofir and Motti Zohar

Topic
Natural Hazards Monitoring, Risk Assessment, Modelling and Management in the Artificial Intelligence Era

Edited by
Dr. Raffaele Albano, Dr. Teodosio Lacava, Dr. Antonietta Varasano, Dr. Ida Giulia Presta, Dr. Mayank Mishra and Dr. Meriam Lahsaini

MDPI

https://doi.org/10.3390/ijgi15080355

International Journal of *Geo-Information*

Article

Spatial Methods for Identifying Undocumented Historical Earthquake Damage

Adi Ofir * and Motti Zohar

School of Environmental Sciences, University of Haifa, Haifa 3103301, Israel; motti.zohar@univ.haifa.ac.il
* Correspondence: adiofir31@gmail.com

Abstract

Historical earthquake records are inherently incomplete: many sites that were likely damaged were never documented, leaving spatial gaps in the macroseismic record. This study evaluates whether intensity values at unreported sites can be estimated from the spatial relationships of surrounding reports, framing the task as a spatial data imputation problem. Three spatial imputation methods, Linear regression, K-Nearest Neighbors (KNN), and Kriging, were applied to eight macroseismic datasets, comprising two historical Dead Sea Transform earthquakes (1927 Dead Sea, 1837 South Lebanon) and six instrumental events from major strike-slip fault systems. Model performance was assessed with 5-fold cross-validation under random and spatial-block designs, using Mean Squared Error (MSE) and success rate, defined as the percentage of predictions falling within ±0.5 and ±1.0 intensity units of observed values. Under random cross-validation, simple and locally focused models performed on par with the complex geostatistical approaches. For the geographically concentrated historical data, success rates reached up to 90% within ±1.0 intensity units. San Andreas events yielded the strongest results among instrumental datasets, while Caribbean events showed the weakest performance due to spatial reporting biases. Under spatial-block cross-validation, performance declined across all models, with linear regression and Universal Kriging proving most robust to spatial extrapolation. These findings provide a methodological basis for estimating intensity at undocumented sites. While continuous intensity mapping from sparse data remains inadvisable, point-based imputation offers a practical tool for enriching historical earthquake records, with direct implications for seismic research along poorly documented fault systems.

Keywords: spatial imputation; macroseismic intensity; historical earthquakes; Dead Sea Transform; KNN; kriging; GIS

Check for updates

Academic Editors: Wolfgang Kainz, Raffaele Albano, Teodosio Lacava, Antonietta Varasano, Ida Giulia Presta, Mayank Mishra and Meriam Lahsaini

Received: 15 April 2026
Revised: 31 July 2026
Accepted: 31 July 2026
Published: 6 August 2026

Copyright: © 2026 by the authors. Published by MDPI on behalf of the International Society for Photogrammetry and Remote Sensing. Licensee MDPI, Basel, Switzerland. This article is an open access article distributed under the terms and conditions of the Creative Commons Attribution (CC BY) license.

1. Introduction

During the last ~130 years since the deployment of the first seismograph [1], data associated with earthquakes and the resulting damage are being measured and collected by instrumental devices worldwide. Unlike the instrumental earthquake data, which provide comprehensive, accurate, and complete information about earthquake occurrences, pre-instrumental records occasionally suffer from inaccuracy, incompleteness, and inconsistency. These deficiencies may concern the source parameters of an earthquake, such as size and location, and also sites that may have been affected yet whose damage was only partially reported or not reported at all. Studies relying solely on such data may not capture the entire seismic influence and activity and will face difficulties examining long-term patterns.

Pre-instrumental data include three main sources: historical records, archeological evidence, and paleoseismological findings. Most of these sources were already collected and gathered in earthquake catalogs [2,3], focused investigations [4–7] and lists [8,9]. The Interpretation and analysis of these sources assist in extracting earthquake occurrences, damage descriptions, and environmental effects. In general, the level of information and the number of reporting sources that are associated with a given event tend to increase the more recently the event occurred. However, additional factors also affect the survival of reports. The first is the importance of the event and the manner in which it was captured in the collective narrative [10]. The second is the administrative and political centrality of a region [11]. Third, the spatial distribution of the population and local literacy rates affect the likelihood of an event being recorded in rural or remote areas [12]. Finally, many original documents were lost to natural decay, fires, or selective archiving over the centuries [13]. Hence, there is a true need to extract the information that was not documented, particularly information associated with the damage and its spread.

This paper explores several spatial techniques for extracting earthquake damage that probably occurred but was not documented, and reviews their advantages, limitations, and associated error rates. The underlying hypothesis is that, given sufficient data, the seismic intensity value at an unreported site can be estimated on the basis of its spatial proximity to reported sites. Furthermore, it can be presumed that if surrounding sites sustained damage, the unreported site likely experienced comparable effects. Thus, by using a methodology that is capable of estimating intensity values with sufficient precision, using spatial relationships exclusively, the hypothesis can be confirmed. By evaluating the performance of these techniques, the study aims to support the enrichment of historical earthquake records of the Dead Sea Transform, where documentation coverage is sparse. To test the accuracy and effectiveness of these techniques, we evaluate them on six well-documented instrumental earthquakes from major strike-slip fault systems alongside two well-documented historical earthquakes associated with the Dead Sea Transform system.

The remainder of the paper is organized as follows. Section 2 describes the eight macroseismic datasets and the pre-processing of the spatial relationships between reporting sites. Section 3 presents the three modeling approaches and the two cross-validation designs used to evaluate them. Section 4 reports the results, comparing the models across events, dataset characteristics, and validation schemes. Section 5 discusses the findings, their limitations, and their applications in historical seismology, and Section 6 concludes.

1.1. Existing Approaches for Detecting Undocumented Earthquake Damage

Pre-instrumental sources may provide invaluable insights, but are often incomplete and unreliable and may therefore be subjected to biases and interpretations [13]. Interpretations of sources may vary widely owing to translation, cultural framing, or a lack of geological verification, increasing the risk of erroneous assessments. Nevertheless, they are almost the only sources available for detecting and characterizing pre-instrumental earthquakes, portraying the spread of the damage, and calculating source parameters such as the epicenter and magnitude [14]. The measurement of earthquakes is a vital tool for risk assessment and future infrastructure planning [15,16], and consistent and unified data are essential for global collaboration in seismic research [17]. Recent developments continue to expand this foundation, including GIS-based frameworks for seismic hazard and vulnerability assessment [18] and the ongoing compilation of long-term historical earthquake archives [19]. In an effort to minimize property damage and prevent loss of life, researchers are actively pursuing methods for predicting and forecasting earthquake events [20]. However, the accuracy of these models depends on the reliability and richness of seismic data across long timeframes. Over time, researchers have developed a variety of

https://doi.org/10.3390/ijgi15080355

methods to reconstruct and enrich incomplete data [21]. These include the generation of synthetic data, interpolation techniques, and data imputation strategies.

Synthetic data models provide a complementary approach to enriching historical earthquake records by simulating plausible seismic scenarios based on physical or spatial rules. These models generate artificial damage locations that resemble observed seismicity in features such as spatial clustering, recurrence intervals, and distance decay. Synthetic data are especially valuable in regions or periods with sparse historical records, as they allow researchers to test hazard scenarios and evaluate the sensitivity of forecasting models under different assumptions. For example, Bakun and Wentworth [22] developed a method to estimate historical earthquake intensity by generating synthetic shaking scenarios calibrated with macroseismic observations. Similarly, Sirovich et al. [23] introduced the Kinematic Function (KF) model, which produces synthetic isoseismal patterns based on fault geometry and slip parameters to infer the source characteristics of historical events.

Extraction and interpolation techniques focus on reconstructing missing or incomplete seismic information by analyzing reported earthquake effects [24]. One of the most widely used methods in this domain is the generation of isoseismal maps, which delineate contours of equal shaking intensity based on macroseismic reports, historical narratives, or archeological evidence. These maps help identify the likely epicentral area, estimate the magnitude, and refine the spatial distribution of damage without instrumental data [25]. Techniques such as kriging and kernel smoothing are employed to interpolate intensity values between known observation points. For instance, one study developed a high-resolution seismic amplification model using regression kriging, integrating seismic station records and geological indicators to map site intensity effects across Switzerland [26]. In another example, a study applied kriging interpolation to macroseismic intensity data from an Italian earthquake, modeling spatial variability with semivariograms and reconstructing a smooth intensity field. The method demonstrated high accuracy even under sparse sampling conditions [27]. More recently, comparative interpolation studies have shown that geostatistical methods such as kriging can produce anomalous intensity zones near the epicenter, and that alternative approaches such as Bayesian Maximum Entropy may offer more consistent results when combined with ground motion prediction equations [28].

1.2. Extracting Undocumented Earthquake Damage

Beyond these traditional methods of data enhancement, another approach to enriching historical damage reports involves the use of “conditional predictions”. Conditional predictions refer to estimates of the intensity value of an undocumented site based on reliable information from a specific event. This information includes reported seismic intensity from neighboring points, distance from the epicenter or the fault system, seismic site effects characteristics, and other factors. Zohar [29] used this technique to survey settlements in the Middle East and count the number of times each settlement was affected by earthquakes throughout history. To this count, he added cases of undocumented damage, based on the proximity of the settlement to verified reports or its location between two verified reports. However, this process must be executed with caution to avoid excessive extrapolation, as Ambraseys [30] and Karcz [31] have demonstrated regarding inflated or misplaced damage reports for the earthquakes of 92 BC, 64 BC, and 749 AD.

The use of conditional predictions has not yet become common in historical earthquake research or the study of historical natural disasters in general. However, it may be conceptualized as a form of data imputation, particularly if unreported locations are understood as missing observations that can be estimated based on spatial patterns. The term “data imputation” refers to a range of techniques for filling in missing data with plausible values, based on observed patterns in the dataset [32]. These techniques include simple methods, such as mean imputation, in which missing values are replaced with the variable's mean [33], and regression imputation, which predicts missing values by relying on statistical relationships with other variables. More advanced approaches, such as multiple imputation (MI) and machine learning-based methods such as MissForest [34], take into account model-dependent uncertainty and complex interactions between variables.

In spatial contexts, imputation methods account for geographical proximity and spatial dependencies. Simple approaches include assigning the value of the nearest spatial neighbor or computing a distance-weighted regional average [35]. More complex spatial models include Conditional Autoregressive (CAR) models, which assume spatial autocorrelation and estimate missing values based on the values of adjacent regions [36], and Kriging, a geostatistical interpolation technique that uses both the distance between observations and their spatial correlation structure (the variogram) to produce accurate local predictions [37]. Within this framework, conditional predictions can be understood as a spatial imputation strategy: estimating the intensity value at an unreported location, conditional on known reports from nearby sites, distance from the seismogenic zone, and other factors.

2. Data Processing

2.1. Earthquake Datasets

Two historical Dead Sea Transform (DST) earthquakes were included in the study: (1) the M6.2 1927 Jericho earthquake [38] and (2) the M7.3 1837 southern Lebanon earthquake [6]. These earthquakes were selected because they provide the largest amount of data, approximately 130 damaged locations each, with an appropriate spatial distribution of damage. For these events, we used the existing macroseismic intensities; both events were assessed on the Medvedev–Sponheuer–Karnik (MSK-64) scale. Today, the macroseismic scale used in the DST region is the European Macroseismic Scale (EMS-98). Damaged locations were also derived from the works of Zohar et al. [39] and Grigoratos et al. [8], who compiled and mapped further historical damage reports across the region. Notably, no site-response corrections were applied to these data. This reflects the nature of macroseismic intensity, which measures observed effects and therefore already incorporates local site effects into the intensity values estimated by the researchers.

For the instrumentally recorded events, data were obtained from the United States Geological Survey (USGS): macroseismic intensity values were collected from the "Did You Feel It?" (DYFI) reports [40], and the epicentral coordinates were taken from the official USGS event catalogs [41]. We examined six well-documented earthquakes from three major strike-slip fault systems. The selected events include (1) the M 7.2 Nippes, Haiti, 2021 earthquake [42], which ruptured the Enriquillo–Plantain Garden fault at a depth of 10 km and led to widespread destruction and displacement in southwestern Haiti, and (2) the M 7.7 earthquake northwest of Lucea, Jamaica, in 2020 [43], which originated 14 km deep along the Oriente Transform Fault and strongly shook the Caribbean region. From the North Anatolian fault system (3) the M 6.1 Düzce, Turkey 2022 earthquake [44] occurred at a shallow depth of 10 km, damaging buildings and injuring dozens, while (4) the M 6.9 Kamariótissa, Greece 2014 [45], event resulted from a strike–slip motion in the North Aegean Trough, causing severe local damage, fatalities, and shaking felt in neighboring countries. From the San Andreas fault system (5) the M 7.1 Ridgecrest, California, 2019 earthquake [46] (depth 8 km, Walker Lane zone) caused hundreds of aftershocks and structural damage, and (6) the M 6.0 South Napa, California, 2014 quake [47] ruptured the West Napa Fault at a depth of 11.3 km, damaging buildings and injuring more than 200 people. These six earthquakes were selected because they occurred recently and generated a large number of responses in the USGS DYFI system, providing a rich dataset of reports for analysis. All DYFI intensities are reported on the Modified Mercalli Intensity (MMI) scale. The eight events are summarized in Table 1, and maps of the spatial distribution of intensity reports for each event are provided in the Supplementary Materials (Figures S4–S10). Detailed spatial datasets for both the historical and instrumental events are available in the accompanying interactive map at https://experience.arcgis.com/experience/bfd0e568b9274f7291121bfd9a84397b (accessed on 30 July 2026).

Table 1. Overview of the eight earthquake datasets. Columns include: Event—event name; Year—year of occurrence; Mw—moment magnitude; Category—historical (H) or instrumental (I); Fault system—the seismogenic fault system associated with the event; Setting—location of the epicenter relative to the coastline (onshore or offshore); Intensity scale—the macroseismic scale of the intensity values; Reports—the number of reports with valid intensity values used in the analysis; Intensity range—the minimum and maximum reported intensities; Data source—the origin of the intensity data. All datasets are available in CSV format via the links in the Data Availability statement.

Event	Year	Mw	Category	Fault System	Setting	Intensity Scale	Reports	Intensity Range	Data Source
South Lebanon	1837	7.3	H	Dead Sea Transform	Onshore	MSK-64	127	4.0–9.0	Ambraseys [6]
Dead Sea (Jericho)	1927	6.2	H	Dead Sea Transform	Onshore	MSK-64	132	3.0–8.5	Avni [38]
Kamariótissa	2014	6.9	I	North Anatolian	Offshore	MMI (DYFI)	131	1.0–9.0	USGS DYFI
South Napa	2014	6.0	I	San Andreas	Onshore	MMI (DYFI)	595	1.0–8.0	USGS DYFI
Ridgecrest	2019	7.1	I	San Andreas	Onshore	MMI (DYFI)	1507	1.0–8.0	USGS DYFI
Lucea	2020	7.7	I	Oriente Transform	Offshore	MMI (DYFI)	373	1.0–7.0	USGS DYFI
Nippes	2021	7.2	I	Enriquillo–Plantain Garden	Onshore	MMI (DYFI)	134	1.0–9.0	USGS DYFI
Düzce	2022	6.1	I	North Anatolian	Onshore	MMI (DYFI)	88	1.0–7.0	USGS DYFI

2.2. Spatial Processing

Each of the damaged locations was georeferenced based on its latitude and longitude and converted into a point feature layer using ESRI© ArcGIS Pro (3.2). To ensure spatial accuracy, the data for each earthquake were projected using the Coordinate Reference System (CRS) of the World Geodetic System 1984 (WGS 84). The earthquake epicenters were projected into the same coordinate system. For events lacking instrumentally determined epicenters, estimated coordinates from the published literature were used. Using ArcGIS tools, two types of spatial relationships were computed: (1) the distance and azimuth (angle) between each damaged location and the epicenter, using the Near tool [48]; and (2) the spatial proximity and azimuth between all damaged locations, using the Generate Near Table function [49]. The complete pre-processing workflow is illustrated in Figure 1.

The intensities at the damaged locations, originally expressed as Roman numerals in their native scales (MSK for the historical events and MMI for the instrumental events), were converted into numerical values for quantitative analysis. Each row in the dataset represents a single neighboring connection, defined as a unique pair of reporting site and its neighbor. The intensity difference, defined as the absolute value resulting from subtracting the intensity value in the damaged location from its spatial neighbor, was calculated and incorporated into the corresponding row (Abs int diff, Table 2). Subsequently, all processed datasets were exported to CSV format for further statistical analysis. This procedure was applied to both the instrumentally reported and historically recorded earthquakes. To account for the differences between expert-assessed historical intensities and crowdsourced DYFI reports, the datasets were treated independently. By modeling each event using its own data, we avoided the potential biases of pooling these distinct data classes or comparing them in raw intensity units. Comparisons between the historical and instrumental groups are therefore limited to model-performance metrics. Table 2 presents an overview of the data frame for the M6.2 Dead Sea earthquake (1927).

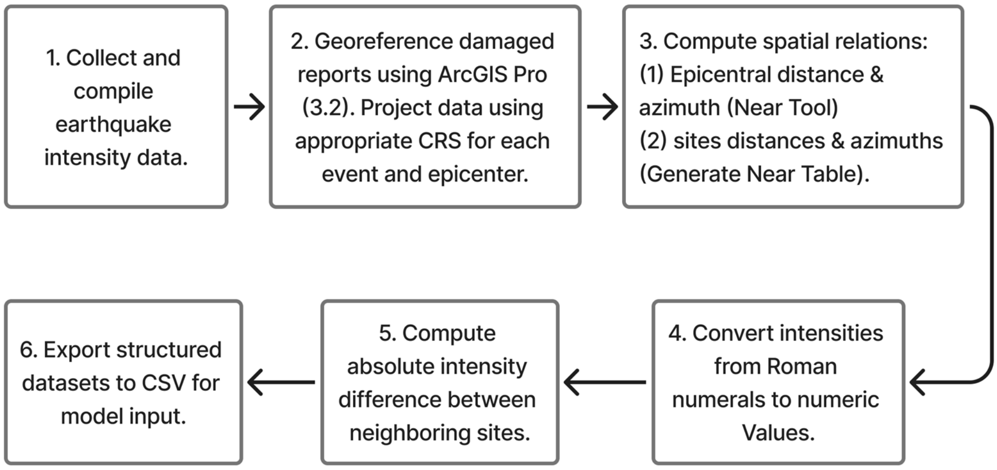

Figure 1. Workflow illustrating the stages of the data processing: (1) Intensity data collection from historical studies and USGS DYFI reports; (2) Georeferencing of damaged locations using ArcGIS Pro with WGS 84 projection; (3) Computation of spatial relationships: epicentral distances and azimuths (angle), and inter-site distances using ArcGIS Near tools; (4) Conversion of intensity values from various seismic scales to numeric values; (5) Calculation of absolute intensity differences between neighboring sites; (6) Export of processed datasets to CSV format for model input.

Table 2. Overview of the data frame of the M6.2 Dead Sea earthquake (1927). The table presents relationships between damaged locations and their neighbors. Columns include: IN FID—identifier of the damaged location; Site—name of the damaged location; Int—reported seismic intensity at the damaged location; Epi dist—distance of the damaged location from the epicenter (km); Epi angle—azimuth (angle) of the damaged location relative to the epicenter (degrees); NEAR FID—identifier of the neighboring location; Near site—name of the neighboring location; Near int, reported seismic intensity at the neighboring location; Near epi dist—distance of the neighboring location from the epicenter (km); Near epi angle—azimuth (angle) of the neighboring location relative to the epicenter (degrees); NEAR DIST—distance between the damaged location and neighboring location (km); NEAR ANGLE—azimuth (angle) from the damaged location to the neighboring location (degrees); Abs int diff—absolute difference in seismic intensity between the damaged location and the neighboring location. In other words, the absolute value results from subtracting the intensity column from the near intensity column.

IN FID	Site	Int	Epi Dist	Epi Angle	NEAR FID	Near Site	Near Int	Near Epi Dist	Near Epi Angle	NEAR DIST	NEAR ANGLE	Abs Int Diff
1	Abu Gosh	6.5	45.9	15	116	Kiriat Anavim	7.0	44.7	14	1.4	49	0.5
1	Abu Gosh	6.5	45.9	15	26	Bet-Sorik	7.0	41.6	14	4.3	30	0.5
1	Abu Gosh	6.5	45.9	15	75	Motza	7.5	41.7	19	4.8	346	1.0
1	Abu Gosh	6.5	45.9	15	98	Ein-Karem	7.0	41.2	21	6.1	338	0.5
1	Abu Gosh	6.5	45.9	15	40	Deir a-Shech	6.5	50.3	21	6.2	242	0.0

https://doi.org/10.3390/ijgi15080355

Table 2. *Cont.*

IN FID	Site	Int	Epi Dist	Epi Angle	NEAR FID	Near Site	Near Int	Near Epi Dist	Near Epi Angle	NEAR DIST	NEAR ANGLE	Abs Int Diff
1	Abu Gosh	6.5	45.9	15	28	Batir	7.0	46.0	26	8.2	290	0.5
1	Abu Gosh	6.5	45.9	15	22	Bet HaKerem	7.0	38.1	20	8.6	352	0.5

2.3. Spatial Data Coverage

Following the data preprocessing steps, differences were observed among the datasets in the number of neighboring connections and the distribution of reported intensities. The mean intensities for the historical events were 7.16 and 6.65 for the 1837 South Lebanon and 1927 Dead Sea events, respectively, while the instrumental events showed mean values ranging from 2.29 to 3.60 (Table 3). The spatial distribution of reports also differed between the two categories. In the historical events, approximately 95–98% of the reports were located within 300 km of the epicenter, with 85–95% of the neighboring-connection distances falling below the 300 km threshold. The spatial distributions of reports associated with the instrumental events were more dispersed than those of the historical events. In five of the six events, 65–90% of reports fell within 500 km of the epicenter. The Lucea 2020 event was an exception with only 20% of the reports within this range, an extreme case of the spatial reporting bias. Neighboring-connection distances also varied: in the 2014 South Napa earthquake, 75% of the connections were below 500 km, while in the 2022 Düzce, 2014 Kamariotissa, and 2019 Ridgecrest earthquakes, only 50–56% of the connections were below 500 km. The Caribbean events, 2021 Nippes and 2020 Lucea, showed the lowest number of neighboring connections, with only 25–32% of these pairs falling within the 500 km distance threshold. This difference in spatial coverage between the two categories is not incidental: it reflects the magnitude-dependent nature of macroseismic attenuation and the difference in documentation. Instrumental events are reported over substantially greater distances than historical events [50]. Accordingly, the distance threshold was set to 300 km for the historical events and 500 km for the instrumental events, matching the distance range over which each data type carries information (Table 3).

Table 3. Summary statistics for the eight datasets of earthquakes. Columns include: Mean Intensity—average seismic intensity reported per event (scales used: MMI for instrumental events, and MSK-64 for the 1837 South Lebanon and the 1927 Dead Sea events); Standard Deviation—variability of reported intensities; Per.Reports—the percentage of total intensity data points located within the defined epicentral distance out of all data points; Per.Neighbor—the percentage of neighboring connections falling within the distance limits out of all neighboring connections. To account for differences in spatial distribution, the distance threshold was defined as 300 km for historical events and 500 km for instrumental events.

Earthquake Dataset	Mean Intensity	Standard Deviation	Per.Reports	Per.Neighbor
1927 Dead Sea	6.65	1.07	98%	95%
1837 S. Lebanon	7.16	1.36	95%	85%
2014 S. Napa	2.86	1.13	85%	75%
2019 Ridgecrest	3.13	1.06	85%	56%
2014 Kamariotissa	3.6	1.53	93%	51%
2020 Lucea	2.29	1.13	18%	32%

https://doi.org/10.3390/ijgi15080355

Table 3. *Cont.*

Earthquake Dataset	Mean Intensity	Standard Deviation	Per.Reports	Per.Neighbor
2021 Nippes	3.18	1.79	72%	25%
2022 Düzce	3.45	1.33	85%	58%

3. Model Implementation

This study aimed to develop and compare three modeling approaches for estimating seismic intensity at unreported locations. Each approach represents a different perspective on spatial dependence: distance decay, neighborhood similarity, and geostatistical autocorrelation. The goal was to evaluate their ability to predict seismic intensity under varying spatial variables and parameters. By doing so, we gained a deeper understanding of the different perspectives and determined their advantages and limitations when estimating intensity values at unreported sites. A conceptual illustration of the three methods is shown in Figure 2, and a detailed description of their implementation is provided in the Supplementary Materials (Figures S1 and S2). The complete pre-processing and modeling pipeline was implemented in Python (v3.9) using ArcGIS Pro (Phase 1), scikit-learn, and PyKrige. The source code is publicly available at https://doi.org/10.5281/zenodo.21786906.

The first model is a linear model (Figure 2a), which examines the relationship between the distance from neighbors and the corresponding seismic intensity difference between them. It is based on the law of distance decay [51,52], which suggests that, on average, the intensity difference increases with distance. Specifically, the model assumes that the mean intensity difference is positively correlated with distance across distance intervals. The second model is a k-Nearest Neighbor (KNN) model, implemented in two variants. The Fixed-k KNN approach (Figure 2b) calculates the predicted intensity as the mean of the k closest neighboring reports (k ranging from 5 to 50), while the Radius-based KNN variant includes all neighboring sites within a predefined radius, computing their average intensity. Formal definitions of the two KNN variants are provided in the Supplementary Materials (Equations (S1) and (S2)).

Both variants operate in accordance with the first law of geography [52], which states that nearby phenomena are more related to each other than distant phenomena. Both the linear and KNN models were tested under varying environmental parameters. These parameters included the distance between neighbors (neighbor distance), the distance from the epicenter (epicentral distance), the angular direction from the epicenter (angular filter, Equation (S3)), and the number of neighbors accounted for in the final prediction (predictor neighbors). Each of the KNN model variants was also tested without spatial filtering, to assess the effect of filtering on model performance. It is important to note that the distance parameters were defined differently for the historical and instrumental earthquakes due to inherent differences in the spatial coverage of observations. In the historical events, the maximum threshold for neighbor distance and epicentral distance was 300 kilometers, whereas in the instrumental events it was extended to 500 kilometers. A detailed description of the environmental parameters, including the full parameter grid (Table S6), is provided in the Supplementary Materials, Chapter 2.

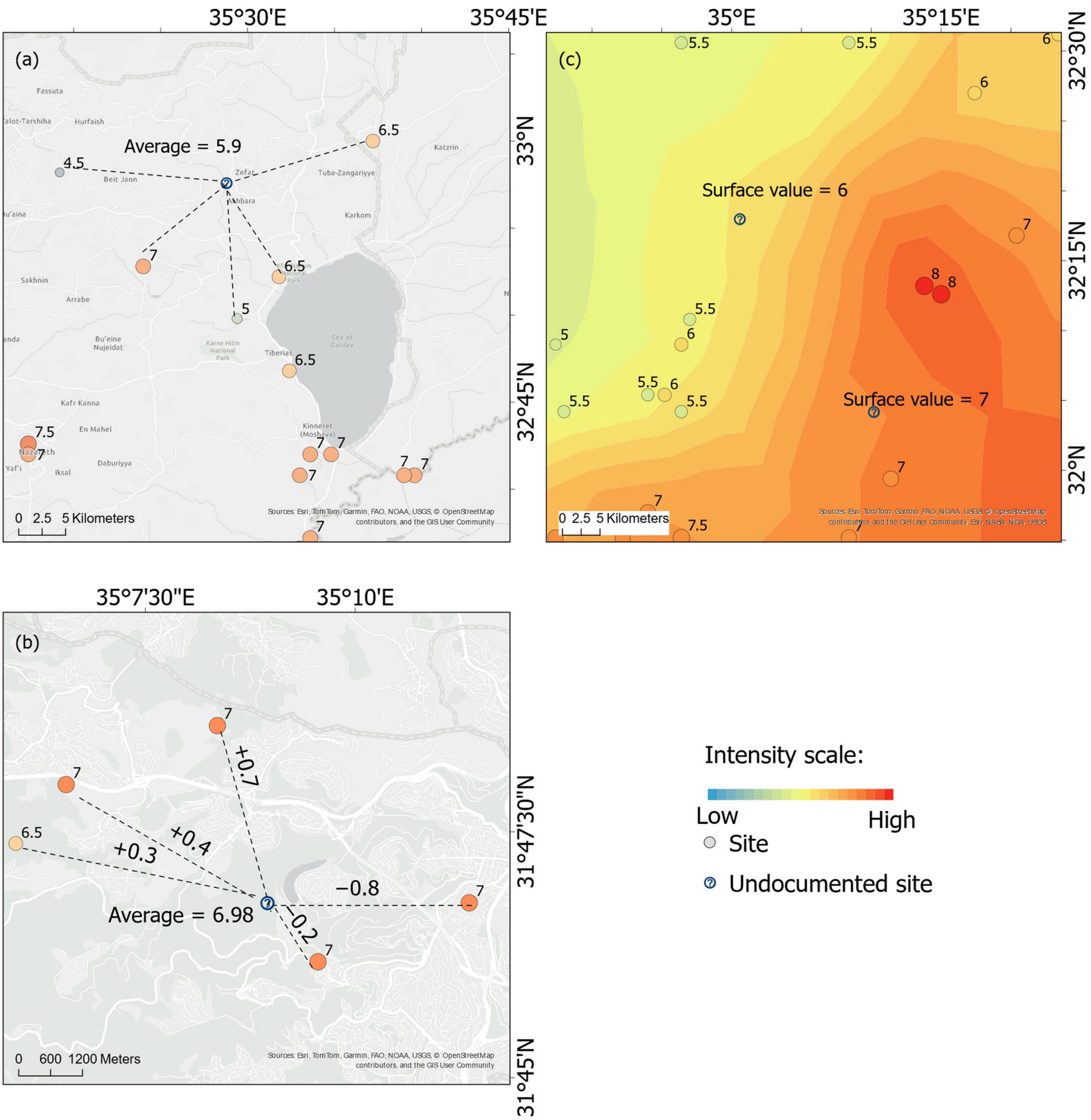

Figure 2. Illustration of the three spatial imputation methods. For this example, data from the 1927 Dead Sea event (MSK-64 macroseismic scale) are used. Colored circles represent reported locations with known intensity values (as shown on labels), while the blue circle containing a question mark indicates the undocumented site. (**a**) Linear Regression Model: Intensity is estimated based on the spatial relationship and distance decay from surrounding sites. The model calculates the intensity difference between the target and each of the nearest neighbors, adjusting for the relative distance from the epicenter (indicated by the ± values), and averages these predictions for the final estimate. (**b**) K-Nearest Neighbors (KNN) Model: The predicted intensity at the undocumented site is calculated as the simple arithmetic mean of the intensity values from its K closest reported neighbors. (**c**) Kriging Model: A geostatistical approach that creates a continuous predicted intensity surface (colored basemap) based on the spatial correlation structure (variogram) of the reported sites. The predicted intensity for any undocumented site is extracted from the interpolated surface value.

The third model is the kriging model [53], a geostatistical method based on the analysis of spatial correlations between intensity values (Figure 2c). Kriging uses the variogram function to estimate spatial similarity between points, calculating optimal weights that ensure an unbiased estimate with minimal error. For each event, the variogram parameters were fitted automatically to the data (least-squares fitting in PyKrige). The environmental parameters were replaced by method-specific parameters, including two kriging types (ordinary and universal), three variogram models (exponential, spherical, and Gaussian), the number of lags, and other model parameters specific to the Kriging type (the number of closest neighbors in ordinary kriging and the drift term in universal kriging).

Each model was evaluated for its predictive accuracy using data from both historical and instrumental earthquakes. The performance of the models was measured using two complementary indicators. The first indicator was the success rate, defined as the proportion of predictions for which the absolute difference between predicted and true seismic intensity values falls within a specified range. Two thresholds were tested for the success rate: ± 0.5 and ± 1.0 intensity units. The lower threshold (± 0.5) reflects the model's ability to reproduce observed values with high precision, while the higher threshold (± 1.0) captures its performance under more flexible accuracy expectations. For example, if an observed intensity of 7 were predicted as 6.6, it would be considered a success under both criteria. In contrast, a prediction of 6.1 would be acceptable only under the ± 1.0 threshold. The second indicator was the Mean Squared Error (MSE), which quantifies the average squared deviation between predicted and observed values, providing a continuous measure of model accuracy while penalizing larger errors more heavily.

To evaluate predictive performance, each model was assessed under k-fold cross-validation (k = 5), in which every site is held out for testing exactly once, and results are averaged across folds. Two partitioning schemes were used. In the random k-fold scheme, sites are assigned to folds at random, while in the spatial-block k-fold scheme, folds are defined as contiguous spatial clusters, so that entire regions are withheld together.

Importantly, because each event was modeled independently, intensity values were not compared across scales. All model training and prediction occurred within a single event and its native scale. Cross-event comparison relied exclusively on performance metrics, which quantify predictive accuracy rather than absolute intensity. As a result, differences between macroseismic scales are unlikely to affect the comparison.

4. Results

4.1. The Model Results

A summary of overall model performance across all eight earthquake datasets under random k-fold cross-validation is provided in Figure 3 (the full results, under both cross-validation schemas, are provided in the Supplementary Materials, Tables S1 and S2). Figure 3 presents the results for five models: the linear model, the two KNN variants, and the two kriging types. For each model and event, the average success rate under the ± 1.0 threshold is presented. This rate represents the percentage of all predictions falling within ± 1.0 intensity units of the observed values. Notably, the simpler models, KNN and linear models, achieve success rates equal to or higher than those of the more complex kriging approaches across most events.

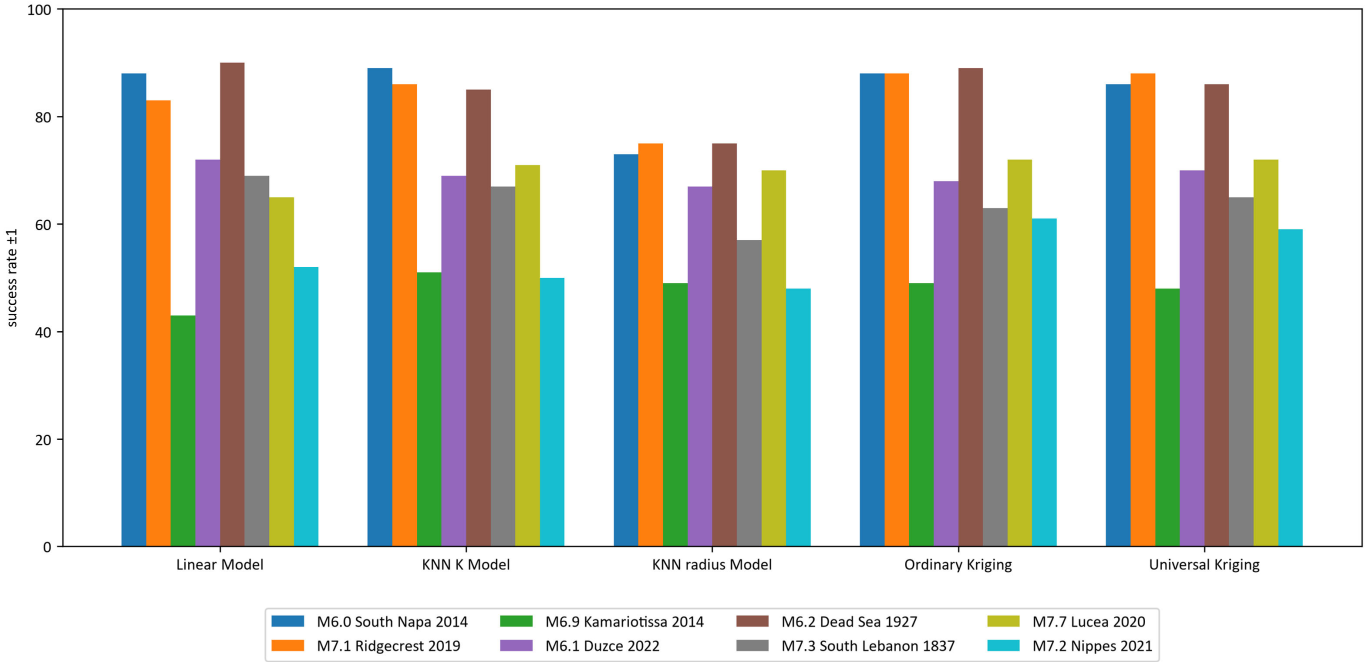

Figure 3. Comparison of model performance across eight earthquakes. The figure displays the performance of five imputation models: Linear Regression model, two K-Nearest Neighbors (KNN) variants (Fixed K and Radius-based), Ordinary Kriging, and Universal Kriging. Performance is measured by the Success Rate ±1.0, defined as the percentage of predicted intensities that fall within ±1.0 intensity units of the observed values.

4.1.1. Linear Regression Model

The linear model demonstrated variable performance across the eight earthquake events. The model achieved its strongest results for the 1927 Dead Sea event, producing an average success rate of 92% within ±1.0 intensity units (64% within ±0.5) and a median MSE of 0.36. The 1837 South Lebanon event showed lower performance, with a success rate of 69% within ±1.0 intensity units and a median MSE of 1.00.

Among the modern events, the 2014 South Napa and 2019 Ridgecrest earthquakes reached 88% and 83% within ±1.0 intensity units (59% and 60% within ±0.5), with median MSE values of 0.48 and 0.40, respectively. The remaining instrumental events showed lower success rates: the 2022 Düzce and 2020 Lucea events reached 72% and 65% within ±1.0 intensity units, respectively, while the 2014 Kamariotissa and 2021 Nippes events reached 43% and 52% within the same threshold, with median MSE values of 2.77 and 1.43.

4.1.2. Fixed-k KNN Models

The Fixed-k KNN model produced success rates broadly comparable to those of the linear model across events. For the historical earthquakes, the model reached 85% within ±1.0 intensity units (59% within ±0.5) for the 1927 Dead Sea event, with a median MSE of 0.49, and 67% within ±1.0 intensity units (38% within ±0.5) for the 1837 South Lebanon event, with a median MSE of 1.16. Among the modern events, the model performed best for the 2014 South Napa and 2019 Ridgecrest events, reaching 89% and 86% within ±1.0 intensity units (60% and 62% within ±0.5) and median MSE values of 0.48 and 0.37, respectively. The 2020 Lucea and 2022 Düzce events reached 71% and 69% within ±1.0 intensity units, respectively, while the 2014 Kamariotissa and 2021 Nippes events reached 51% and 50% within the same threshold, with median MSE values of 2.69 and 2.23.

4.1.3. Radius-Based KNN Model

The Radius-based KNN model generally showed lower success rates than the fixed-k variant across all events, illustrated in Figure 3. For the historical earthquakes, this pattern was particularly evident. The 1927 Dead Sea earthquake reached 75% within ± 1.0 intensity units (43% within ± 0.5), with a median MSE of 0.75. The 1837 South Lebanon event showed poor results, with 57% within ± 1.0 intensity units (26% within ± 0.5), and a median MSE of 1.32. This pattern of reduced accuracy persisted across the instrumental events: success rates within ± 1.0 intensity units ranged from 48% (2021 Nippes) to 75% (2019 Ridgecrest), with median MSE values ranging from 0.59 to 2.84.

4.1.4. Kriging Interpolation

Ordinary kriging (OK) and universal kriging (UK) were evaluated using spherical and exponential variograms. The Gaussian variogram results were excluded due to unstable computations, characterized by extremely high MSE values and large standard deviations across all parameter combinations. For the historical earthquakes, kriging produced its strongest results for the 1927 Dead Sea earthquake, where OK reached 89% within ± 1.0 intensity units (73% within ± 0.5) with a median MSE of 0.29, and UK reached 86% within ± 1.0 intensity units (67% within ± 0.5) with a median MSE of 0.27. The 1837 South Lebanon event reached 63% (OK) and 65% (UK) within ± 1.0 intensity units, with median MSE values of 1.19 and 1.12, respectively. Among the instrumental events, the 2014 South Napa event reached 88% (OK) and 86% (UK) within ± 1.0 intensity units, and the 2019 Ridgecrest event reached 88% under both kriging types (63% within ± 0.5). The four remaining instrumental events reached success rates within ± 1.0 intensity units ranging from 48% to 72%, with median MSE values between 0.86 and 2.53. Across the configurations, the spherical and exponential variograms produced similar results.

4.1.5. Comparison Across Model Families

A direct comparison of the three model families shows that the best-performing simpler model (linear model or Fixed-k KNN) and the best-performing kriging model differed by an average of 0.2 percentage points within ± 1.0 intensity units across the eight events. The simpler models matched or exceeded kriging in five of the eight events. The largest difference in favor of a simpler model was 4 percentage points (1837 South Lebanon), and the largest difference in favor of kriging was 9 percentage points (2021 Nippes). Across all five models, the spread between the highest and lowest success rate within a single event averaged 11.1 percentage points, ranging from 5 to 16 percentage points. A Wilcoxon signed-rank test across the eight events found no statistically significant difference between any simpler model (linear or Fixed-k KNN) and any kriging model (OK or UK) under either cross-validation scheme ($p \geq 0.14$ in all pairwise comparisons).

4.2. Comparison Between Dataset Characteristics

The datasets differ in the spatial distribution of their reports. Three groupings were used to examine how this variation relates to model performance: the distinction between historical and instrumental events, the distinction between onshore and offshore epicenters, and the comparison between the two cross-validation schemes.

4.2.1. Historical and Instrumental Datasets

The datasets were grouped into historical and instrumental categories, and the average success rates were calculated for each group. This grouping isolates the effect of data characteristics on the models: spatially concentrated, narrow-range historical reports versus dispersed, wide-range instrumental reports. The linear model achieved average success rates of 80% for the historical events and 67% for the instrumental events within ±1.0 intensity units (52% and 42% within ±0.5). The Fixed-k KNN model showed a similar trend, with 76% for the historical and 69% for the instrumental events within ±1.0 intensity units (49% and 45% within ±0.5), while the Radius-based KNN model reached 66% and 64% within ±1.0 intensity units (35% and 40% within ±0.5). OK reached 76% for the historical and 71% for the instrumental events within ±1.0 intensity units (56% and 44% within ±0.5), and UK reached the same values within ±1.0 intensity units (54% and 45% within ±0.5). All five models reached higher success rates on the historical group than on the instrumental group. This comparison is broken down by individual parameter settings in Figures 4–6, which show the grouped success rates under random k-fold cross-validation, for the linear, Fixed-k KNN, and OK models (underlying values in Supplementary Tables S3 and S4).

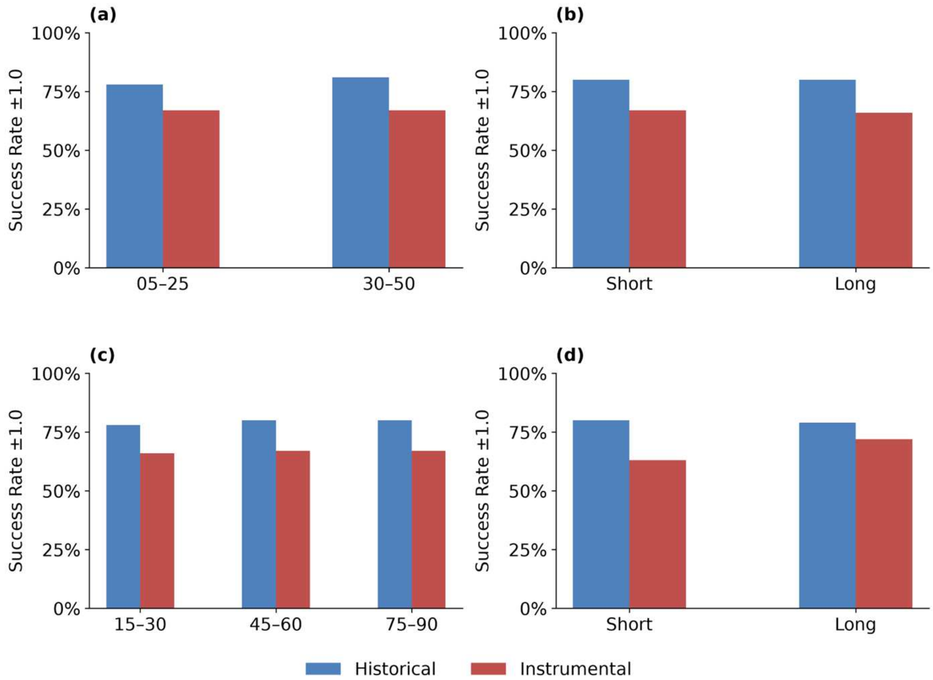

Figure 4. Average success rates within ±1.0 intensity units under random k-fold cross-validation for the linear regression model, grouped by spatial parameters: (**a**) number of predictors, (**b**) neighbor distance, (**c**) angular range, and (**d**) epicentral distance. Results comparing historical earthquakes (blue) and instrumental earthquakes (red). Each bar represents the mean performance of parameter groups across all earthquakes.

4.2.2. Onshore and Offshore Events

The datasets were additionally grouped by the location of the epicenter relative to the coastline into onshore events (1927 Dead Sea, 1837 South Lebanon, 2014 South Napa, 2019 Ridgecrest, 2022 Düzce, and 2021 Nippes) and offshore events (2014 Kamariotissa and 2020 Lucea). Notably, the offshore group comprises only two events, both of which are sparsely reported. Within ±1.0 intensity units, the linear model reached 76% for the onshore events and 52% for the offshore events (49% and 30% within ±0.5) (Figure 7; underlying values in Table S5). The Fixed-k and Radius-based KNN models reached 75% and 66% for the onshore events and 59% and 58% for the offshore events, respectively. OK and UK both reached 76% for the onshore events, and 61% and 60% for the offshore events, respectively. Across all models, the onshore events showed higher success rates than the offshore events, with the largest difference for the linear model (24 percentage points) and the smallest for the Radius-based KNN model (8 percentage points).

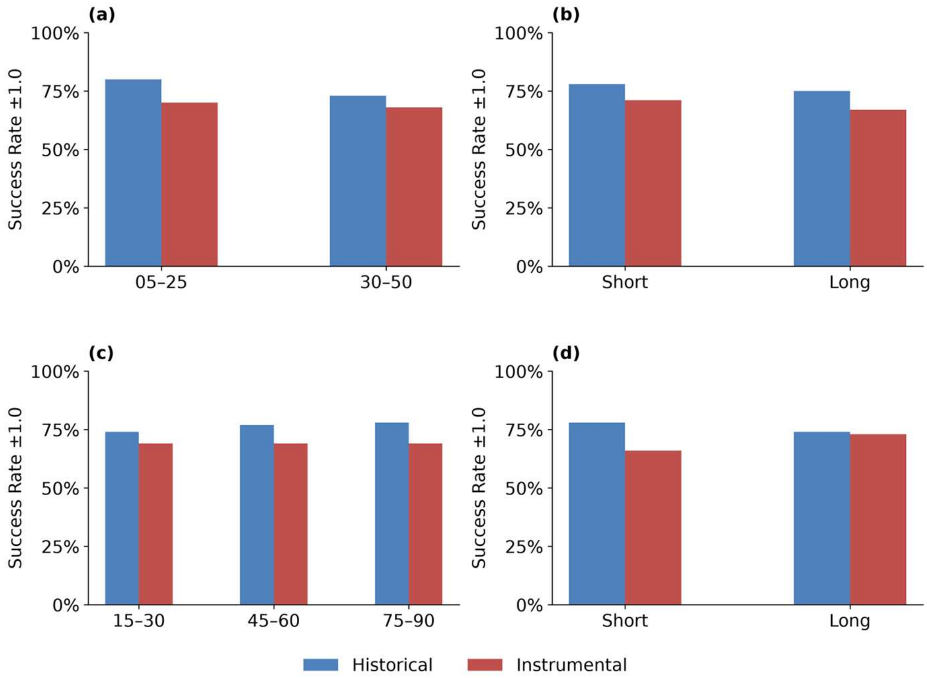

Figure 5. Average success rates within ±1.0 intensity units under random k-fold cross-validation for the KNN fixed-k model, grouped by spatial parameters: (**a**) number of predictors, (**b**) neighbor distance, (**c**) angular range, and (**d**) epicentral distance. Results comparing historical earthquakes (blue) and instrumental earthquakes (red). Each bar represents the mean performance of parameter groups across all earthquakes.

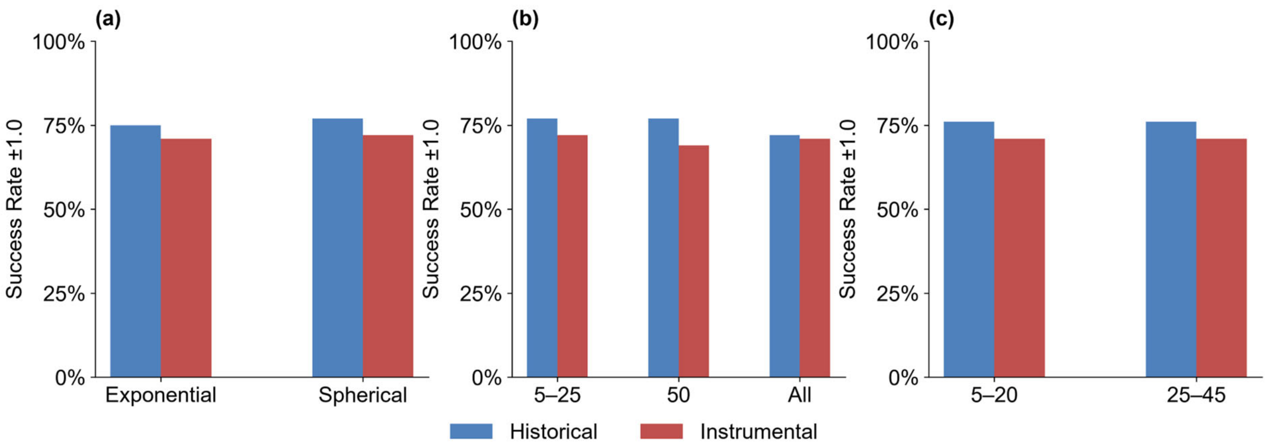

Figure 6. Average success rates within ±1.0 intensity units under random k-fold cross-validation for the Ordinary Kriging model, grouped by model parameters: (**a**) number of points used for prediction (n_closest), (**b**) lag number, and (**c**) variogram model. Results comparing historical earthquakes (blue) and instrumental earthquakes (red). Each bar represents the mean performance of parameter groups across all earthquakes.

4.2.3. Random and Spatial-Block Cross-Validation

Success rates were lower under spatial-block cross-validation than under random k-fold for every model and every event (Table 4). The magnitude of the decrease differed markedly between models. Averaged across the eight events, the linear model and UK showed the smallest decreases (13.8 and 15.3 percentage points, respectively), while the Fixed-k KNN model showed the largest (21.0 percentage points).

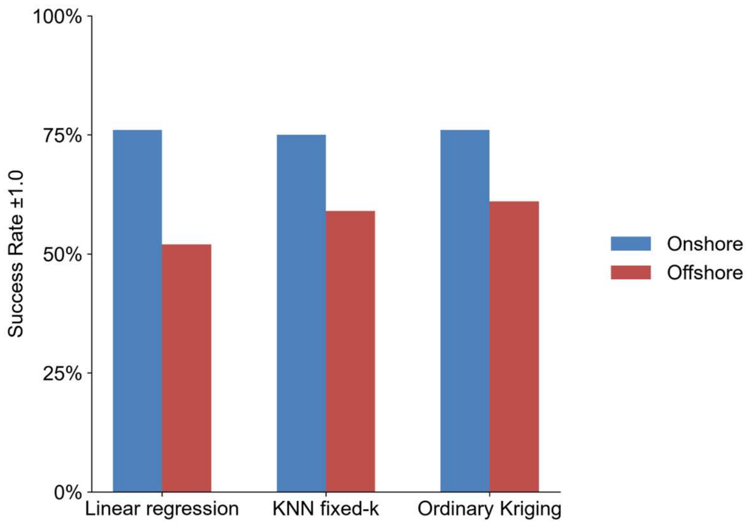

Figure 7. Average success rates within ±1.0 intensity units under random k-fold cross-validation, comparing onshore earthquakes (blue) and offshore earthquakes (red) across three models: linear regression, fixed-k KNN, and Ordinary Kriging. Each bar represents the mean performance across all earthquakes in the group.

Table 4. Success rates within ±1.0 intensity units under random k-fold and spatial cross-validation, shown as random/spatial for each model and event. The final row gives the mean decrease from random to spatial-block cross-validation, in percentage points, across all eight events.

Earthquake	Linear	Fixed-k KNN	Radius KNN	Ordinary Kriging	Universal Kriging
1927 Dead Sea	90/82	85/49	75/46	89/55	86/58
1837 South Lebanon	69/63	67/44	57/39	63/35	65/47
2014 South Napa	88/68	89/57	73/50	88/67	86/69
2019 Ridgecrest	83/74	86/72	75/66	88/64	88/66
2014 Kamariotissa	43/35	51/39	49/38	49/36	48/38
2022 Düzce	72/57	69/59	67/58	68/56	70/58
2021 Nippes	52/35	50/27	48/24	61/54	59/56
2020 Lucea	65/36	71/53	70/52	72/53	72/60
Mean decrease	−13.8	−21.0	−17.5	−19.8	−15.3

The differences were most pronounced for the spatially concentrated events. For the 1927 Dead Sea event, the success rate within ±1.0 intensity units decreased from 90% to 82% for the linear model, from 85% to 49% for the Fixed-k KNN model, and from 89% to 55% for OK. For the 2014 South Napa event, the corresponding values decreased from 88% to 68% (linear), from 89% to 57% (Fixed-k KNN), and from 88% to 67% (OK). The 2019 Ridgecrest event, the most densely reported dataset, showed the smallest decreases: from 83% to 74% (linear) and from 86% to 72% (Fixed-k KNN).

The spread between models also widened under spatial-block cross-validation. Within a single event, the difference between the highest and lowest-performing models averaged 11.1 percentage points under random k-fold and 19.5 percentage points under spatial-block cross-validation, ranging from 3 to 36 percentage points. Under random k-fold, the best simpler model and the best kriging model differed by an average of 0.2 percentage points, whereas under spatial-block cross-validation this difference averaged 2.6 percentage points, with individual events ranging from 24 percentage points in favor of the linear model (1927 Dead Sea) to 21 percentage points in favor of UK (2021 Nippes).

For the events with the fewest reporting sites and the widest spatial dispersion (2021 Nippes and 2020 Lucea), the spatial-block partitioning did not produce five populated blocks, and the effective number of folds was reduced accordingly. Spatial-block results for these two events are therefore based on a smaller number of tested sites than the corresponding random k-fold results.

5. Discussion

This study evaluates the performance of three imputation models—linear, KNN, and kriging—using eight macroseismic earthquake datasets comprising historical and instrumental events. The three models were evaluated under two cross-validation schemes, using Mean Squared Error (MSE) values and Success Rates within thresholds of ± 0.5 and ± 1.0 intensity units. These metrics were used to reveal trends potentially related to data quality, sample size, data distribution, and model complexity. These trends offer valuable insights into the advantages and limitations of imputation approaches for detecting earthquake damage that occurred but was not documented, thus supporting ongoing efforts to enrich historical earthquake records where data coverage is limited.

5.1. Impact of Data Quality and Quantity

The models' performance depends heavily on data quality and quantity. Where datasets were large, high-quality, and spatially well-distributed, as in the San Andreas-related earthquakes (2014 South Napa and 2019 Ridgecrest), the models achieved meaningful results, reaching an average success rate of 85%. In contrast, the sparse reporting over a relatively large area in events such as the 2014 Kamariotissa event restricted the models' ability to capture spatial patterns, which may partly account for the poor performance across methods.

The quality of the spatial distribution, along with dataset size, may explain the suboptimal results in the 2021 Nippes event (54% average success rate). Bossu et al. [54] noted that participation in citizen-seismology projects such as DYFI or the European-Mediterranean Seismological Centre (EMSC) is strongly influenced by internet penetration and accessibility. Caribbean regions, with limited access or low awareness, tend to contribute fewer reports to these systems, while the US, lying within the same sensing range, adds a large number of remote reports to these earthquake datasets. As a result, the Caribbean datasets exhibit spatial bias, with most reports originating from distant locations while local reports are sparse. Consequently, the models appear to have been driven by distant rather than local patterns, suggesting that a large dataset does not compensate for spatial bias and may even increase prediction error when geographic coverage is skewed.

It is worth noting that DYFI reports undergo aggregation and binning by the USGS before release, which might be expected to yield spatially smoother fields that are easier to predict from neighbors. However, the instrumental datasets did not show higher predictive success than the concentrated historical data; on the contrary, their dispersed and spatially biased coverage produced lower success rates. DYFI smoothing therefore provides no advantage for spatial imputation. Performance is controlled by spatial coverage and bias, not by the crowdsourced origin of the data.

Interestingly, the opposite pattern emerges under concentrated reporting conditions for the historical earthquakes. Despite its limited but geographically concentrated data, the 1927 Dead Sea event yielded the strongest results, with an average success rate of 85% within ± 1.0 intensity units and median MSE values of 0.27–0.75 across models. This trend may be explained by two factors: spatial concentration and reduced variability. The reports are confined to relatively small areas, so even strict distance thresholds (e.g., 300 km) remove little of the available information. This concentration of damage reports suggests a reduction in noise, potentially enabling more accurate local predictions. In addition, the historical intensity values typically span a small range, since only moderate to severe shaking was documented (mean intensities 6.65–7.16, SD 1.07–1.36), whereas the instrumental events include a large number of low recorded intensities (mean 2.29–3.60, SD 1.06–1.79). This narrow intensity range tends to reduce statistical variability, which may partly explain the higher accuracy of the models applied to the historical events. Notably, the 1927 Dead Sea outperforms the 1837 South Lebanon, possibly because the more recent event benefits from more reliable documentation, whereas the 1837 historical records are perhaps less precise.

5.2. Spatial Coverage of Reports as the Principal Constraint

The results indicate that the spatial arrangement of the surviving reports, rather than their number, is the principal constraint on what these models can recover. All models predict intensity at an undocumented site by drawing on the reports that surround it. Where such reports exist in the immediate vicinity, the models perform comparably well; where they do not, prediction accuracy degrades regardless of how many reports exist elsewhere in the dataset. In other words, a site that lies beyond the reported area cannot be informed by it, and no choice of model recovers information that the data do not contain.

The two cross-validation schemes used here make this constraint explicit. Random k-fold withholds individual sites while leaving the surrounding reports in place, so that each withheld site remains embedded within the reported field. Spatial-block k-fold withholds contiguous regions, so that entire areas are left unreported, and the withheld sites must be predicted from reports that lie outside the region. Success rates were lower under Spatial-block cross-validation for every model and every event (Table 4), with average decreases of 13.8 to 21.0 percentage points. The comparison of random and spatial partitioning follows established practice in spatial modeling, where random cross-validation is known to yield optimistic performance estimates because training and test observations remain spatially dependent [55–57]. The spatial-block partitioning used here follows the k-means clustering approach of Brenning [58], although it should be noted that the appropriate choice between the two schemes remains debated [59].

The decrease was largest for the spatially concentrated events. For the 1927 Dead Sea event, withholding contiguous blocks reduced the success rate within ± 1.0 intensity units from 85% to 49% for the fixed-k KNN model and from 89% to 55% for OK, while the linear model declined only from 90% to 82%. The 2019 Ridgecrest event, the most densely reported dataset in this study, showed the smallest decreases across models. The 2020 Lucea event illustrates the same constraint from the opposite direction: it performs adequately under random partitioning (70% average success rate), yet the linear model declines from 65% to 36% under spatial-block partitioning, the steepest decline of any event. Its reports are numerous but confined to a narrow, distant band, so once a contiguous region is withheld, few informative neighbors remain. Report density, rather than report count, therefore governs whether an undocumented site can be estimated at all.

The comparison between onshore and offshore events extends this observation to a permanent, structural form of the same limitation. Offshore epicenters are surrounded on one or more sides by an area that can never be reported, since macroseismic intensity is defined by observed effects on people and structures. The two offshore events in this study (2014 Kamariotissa and 2020 Lucea) reached average success rates of 52–61% within ± 1.0 intensity units, compared with 66–76% for the six onshore events, with the largest difference recorded for the linear model (76% versus 52%). Although this comparison rests on only two offshore events, both sparsely reported, it is consistent with the spatial-block cross-validation results: an offshore epicenter imposes on the reported field the same condition that spatial-block cross-validation partitioning imposes artificially. Spatial imputation of macroseismic intensity is therefore poorly suited to offshore events, and its application to such settings should be treated with caution.

This constraint bears directly on older earthquakes, for which only limited macroseismic reports exist. Under such conditions, imputation models can become less effective, as spatial structure may be difficult to infer and parameters such as the variogram range or the number of neighbors lose meaning. The spatial-block results in this study quantify that difficulty directly: for the two events with the fewest reporting sites, contiguous blocks could not be formed without leaving folds unpopulated, and success rates declined most steeply. Simple and local approaches, such as KNN or a linear model with a small, fixed number of neighbors, may still provide qualitative insights into possible intensity patterns, whereas kriging could potentially introduce artificial continuity that might not be supported by the data. At the same time, high data quality can partly compensate for a small sample size. When a few reliable observations are well distributed in space, prediction remains possible and may be more accurate than results from a large but poorly structured dataset, as the contrast between the 1927 Dead Sea and 2020 Lucea events illustrates. Consequently, extremely sparse historical datasets should not be used to produce continuous intensity maps but may still be useful for estimating seismic intensity at individual points.

5.3. Model Complexity and Parameter Settings

Under random k-fold cross-validation, the simpler models performed on par with the geostatistical approaches. The best simpler model and the best kriging model differed by an average of 0.2 percentage points within ± 1.0 intensity units across the eight events, and the simpler models matched or exceeded kriging in five of the eight events. The largest difference in favor of a simpler model was 4 percentage points (1837 South Lebanon) and the largest in favor of kriging was 9 percentage points (2021 Nippes).

This equivalence carries a practical implication. If the objective is to estimate intensity at an individual site, a geostatistical interpolator offers no measurable advantage over a linear distance–decay model or an average of the nearest reported neighbors. The additional structure of kriging does not translate into higher predictive accuracy under these data conditions. The Wilcoxon tests confirm that the observed differences are not statistically distinguishable. This finding is consistent with reports that kriging does not consistently outperform simpler interpolators for seismic intensity fields [28] and with the observation that kriging offers little advantage over simpler methods where spatial autocorrelation is weak, or the sampling is irregular [60,61]. It also aligns with Pisarenko and Pisarenko [62], who proposed a modified KNN algorithm that provides statistically robust intensity fields without prior regionalization or normalization, making it well-suited for heterogeneous or sparse datasets.

The equivalence holds, however, only where reports surround the target site. Under spatial-block cross-validation, the models diverge. Within a single event, the gap between the best and the worst model widens from 11.1 percentage points on average under random partitioning to 19.5% points under spatial-block partitioning. All models lose accuracy when whole regions are withheld, but not to the same degree. Averaged across the eight events, the linear model falls by 13.8% points and UK by 15.3%, while the Fixed-k KNN model falls by 21% points. The two most robust models share a global component: an explicit distance–decay relationship in the linear model and a deterministic drift term in UK. The Fixed-k KNN model estimates sites from their nearest reported neighbors alone. When no reported site lies nearby, a global component still yields an estimate, while a local average has nothing to average. Similar contrasts have been reported in other settings characterized by discontinuous spatial variation. In such cases, models incorporating a regression or trend component outperform purely distance-based interpolators, since the nearest observation is not necessarily the most similar [60]. Model choice matters most where the data are least informative, and least where they are most informative. Kriging assumes stationarity of the mean and of the second-order moments, a condition that fields shaped by singular processes frequently violate [63], and that reporting bias in historical catalogs further undermines [27].

Among the variogram models tested, the spherical and exponential variograms produced comparable results, and OK performed similarly to UK under random partitioning, as expected where the data carry no pronounced regional trend [64]. UK proved more robust under spatial-block partitioning, consistent with the role of its drift term as a global constraint. Similarly, the linear model and Fixed-k KNN model achieved higher success rates than the Radius-based KNN model across events, as they avoid the noise introduced by an unbounded neighbor count. The comparable performance of the Fixed-k KNN model even in the large Ridgecrest dataset suggests that complex geostatistical models are not necessarily superior for large datasets, echoing comparisons in which kriging and inverse distance weighting achieved equivalent accuracy across a wide range of sampling densities [61]. Overall, these findings support the feasibility of using simple spatial models for seismic intensity estimation at individual sites, especially when data quality or spatial coverage is limited.

The same conditionality applies to parameter settings within each model. Under random k-fold cross-validation, where reported sites surround each target location, parameter settings had a limited effect (Figures 4–6). When reports are densely interspersed, most reasonable parameter configurations recover a similar signal, and the choice among them is of secondary importance.

Under spatial-block cross-validation, the picture changes; the angular filter shows this most clearly. Widening the angular range from 15–30° to 75–90° altered the success rate by eight percentage points. Where a whole region is unreported, a narrow angular window discards neighbors that carry information about that region, whereas the same window is harmless when neighbors are available in every direction.

One parameter behaved differently between the historical and instrumental datasets under both schemes. Success rates declined slightly with increasing epicentral distance for the historical events, from 80% to 79%, while for the instrumental events they increased, from 63% to 72% (Figures 4d and 5d; Table S3). This likely reflects the differing composition of the two categories. Historical reports are concentrated near the epicenter and describe moderate to severe shaking, whereas instrumental reports extend to large distances, where low, spatially smooth intensities dominate and are more easily predicted. In practical terms, parameter selection should be guided by data density: where reporting is dense, the choice matters little, and where it is sparse, wider angular ranges and larger neighbor sets preserve the limited information available.

5.4. Implications for Historical Seismology Research

The imputation framework presented here has applications in historical seismology beyond the reconstruction of individual intensity values. The first application is at the level of event cataloging. Spatial models can help identify settlements likely to have been affected by a given earthquake, extending frequency-based analyses of how often individual localities were impacted across historical time [29]. The second application is the qualitative characterization of an earthquake's felt area, where imputed values may indicate that shaking extended across a broader region than the surviving reports alone suggest. The third application is methodological guidance for archival and field research: by highlighting localities that models suggest were likely affected yet lack documentation, the framework can help prioritize where further examination of historical sources may be most productive. The fourth application is the corroboration of uncertain reports. Historical catalogs include damage entries flagged as doubtful or of low reliability. Where a model independently predicts an intensity consistent with such a report, the spatial agreement provides additional information that can raise confidence in the entry. Conversely, a marked spatial inconsistency may indicate that the report warrants further scrutiny [30,31].

5.5. Limitation and Future Directions

Given the preliminary nature of this study and its defined scope, several limitations should be acknowledged. The first limitation concerns the source of the intensity data. The macroseismic intensities were assigned by the original researchers, who interpreted historical accounts and assessed the intensity at a given site. We adopted these assessments as-is; the analysis therefore inherits the interpretive uncertainty present in the original estimates, which are not always precise. The choice of macroseismic scale is secondary in this respect: the historical events were assessed on the MSK scale, and the instrumental events on the MMI scale, and these scales are approximately equivalent across the intensity range that characterizes the datasets [65]. Combined with the fact that intensities were never compared across scales, this study does not examine the effects of scale differences on the results. The historical analysis was limited to only two earthquakes on the DST due to the lack of reliable databases for older events. Because both events share the same region, the transferability of the results to other regions remains untested. The six instrumental events were included partly to address this constraint, exposing the models to a wider range of spatial coverage and data density than the historical record alone provides. Nevertheless, expanding the historical earthquake database analysis and conducting further intensity assessments would enhance future work. Modern crowdsourced datasets also present challenges: outside the US, DYFI participation is biased by internet access and population density, particularly affecting the Caribbean earthquakes in this study.

Finally, missingness in historical macroseismic records is not random: the survival of a report reflects settlement patterns, archival coverage, and documentation practices. The estimates produced here are therefore conditional on the observed reporting pattern, and the spatial-block cross-validation was designed to probe this structured missingness. Masking schemes based on settlement or documentary-coverage proxies remain a direction for future work.

Beyond the data constraints, this study focused on spatial relationships alone and did not incorporate the physical factors of ground motion prediction equations or fault rupture models, which could provide valuable information. This reflects the study's scope and methodological aim: to evaluate what can be calculated from spatial structure using GIS-operable layers, without physical models. Additionally, no explicit site-response corrections were applied: macroseismic intensity is a measure of observed effects, so local site effects are already embedded in the assigned intensity values. Moreover, because any such physical effect would impact all models systematically in the same way, its omission is unlikely to change the comparative results between the linear, KNN, and kriging models. Incorporating explicit physical covariates is a natural extension for future work.

Furthermore, several methodological choices limited the analysis. Rather than searching for a single optimal configuration, the models were evaluated across a fixed grid of parameter settings, and the results were averaged across it: some parameter combinations remain untested. As this research focused on basic spatial techniques, only three modeling approaches were tested. For instance, inverse distance weighting (IDW) could serve as a direct benchmark for the distance-weighting effects identified here, while ensemble methods might better handle the spatial heterogeneity observed in the Caribbean datasets.

6. Conclusions

This study partially confirms the hypothesis that seismic intensity at undocumented sites can be estimated from the spatial relationships among sites with documented damage. By applying the linear, KNN, and kriging models across diverse datasets, we demonstrated that spatial relationships provide a considerable basis for data imputation. The resulting success rates, reaching up to 90% within ±1.0 intensity units, support the hypothesis that neighboring sites might experience comparable seismic effects, thereby offering a useful framework for enriching sparse historical records of earthquake damage.

The comparative analysis between the models revealed that model complexity is not necessarily the decisive factor when dealing with macroseismic data. In contrast to the assumption that complex geostatistical models are superior, this research shows that simpler approaches such as KNN and the linear model demonstrate performance equivalent to kriging, particularly where the data is geographically concentrated. Their advantage is practical rather than statistical; they achieve comparable accuracy with less modeling effort. This pattern points to spatial concentration, not sample size, as the decisive factor. Large instrumental datasets cover more ground but carry more noise and reporting bias. In contrast, the concentrated, high-intensity character of the historical records allows for accurate local predictions despite small sample sizes.

Given the preliminary nature of this study, the analysis prioritized surveying simple models, a limited range of parameters, and few datasets rather than fully optimizing any single approach, thereby laying the foundation for continuing future work.

Finally, this research supports the integration of "conditional predictions" into historical seismology by providing a methodological basis for estimating intensity at undocumented sites. Although sparse datasets cannot generate continuous intensity surfaces, extracting intensity at individual sites enables a more complete analysis of past seismic events. Beyond individual intensity estimates, this approach can help target archival and archaeo-seismological research by identifying localities where earthquake effects are indicated by the models but absent from the surviving documentation. These results provide a scalable tool for researchers to fill documentation gaps, which may help refine seismic hazard assessments in regions such as the DST, where understanding the true extent of historical damage is critical for future research.

Supplementary Materials: The following supporting information can be downloaded at: https://www.mdpi.com/article/10.3390/ijgi15080355/s1, Figure S1: Linear regression and KNN workflow; Figure S2: Kriging workflow; Figure S3: Spatial relationships between reported sites, epicenter and neighbours; Figure S4: Intensity reports, 2022 Düzce; Figure S5: Intensity reports, 2014 Kamariótissa; Figure S6: Intensity reports, 2020 Lucea; Figure S7: Intensity reports, 2021 Nippes; Figure S8: Intensity reports, 2014 South Napa; Figure S9: Intensity reports, 2019 Ridgecrest; Figure S10: Intensity reports, 1837 South Lebanon and 1927 Dead Sea; Table S1: Model performance under random k-fold cross-validation; Table S2: Model performance under spatial-block cross-validation; Table S3: Success rates by parameter group, linear and fixed-k KNN models; Table S4: Success rates by parameter group, Ordinary Kriging; Table S5: Success rates by epicentral setting; Table S6: Parameter grid, Dataset S1: Raw macroseismic intensity data for the eight earthquakes (ZIP archive of eight CSV files—Data.zip).

Author Contributions: Conceptualization, Adi Ofir and Motti Zohar; methodology, Adi Ofir; software, Adi Ofir; validation, Motti Zohar; formal analysis, Adi Ofir; investigation, Adi Ofir; data curation, Adi Ofir; writing—original draft preparation, Adi Ofir; writing—review and editing, Motti Zohar; visualization, Adi Ofir; supervision, Motti Zohar; project administration, Adi Ofir. All authors have read and agreed to the published version of the manuscript.

Funding: This research received no external funding.

Data Availability Statement: The raw macroseismic intensity datasets analysed in this study are provided in the Supplementary Materials. The complete model output tables, covering all parameter configurations, cross-validation schemes and folds, are archived at https://doi.org/10.5281/zenodo.21787556. The source code used to generate them is archived at https://doi.org/10.5281/zenodo.21786906. The instrumental intensity data were obtained from the USGS "Did You Feel It?" system, and the historical intensity assessments were compiled from the published sources cited in Section 2. The spatial datasets can also be explored through the interactive map at https://experience.arcgis.com/experience/bfd0e568b9274f7291121bfd9a84397b (accessed on 30 July 2026).

Acknowledgments: The authors thank Lian Amir, Aviv Oppenheim, Noa Shamir, and Jefferson Williams of the GIS Lab at the University of Haifa for their support, comments, and constructive criticism throughout this work.

Conflicts of Interest: The authors declare no conflict of interest.

References

1. Davison, C. *The Founders of Seismology*; Cambridge University Press: Cambridge, UK, 1930.
2. Ambraseys, N. *Earthquakes in the Mediterranean and Middle East: A Multidisciplinary Study of Seismicity Up to 1900*; Cambridge University Press: Cambridge, UK, 2009.
3. Guidoboni, E.; Ferrari, G.; Tarabusi, G.; Sgattoni, G.; Comastri, A.; Mariotti, D.; Ciuccarelli, C.; Bianchi, M.G.; Valensise, G. CFTI5Med, the New Release of the Catalogue of Strong Earthquakes in Italy and in the Mediterranean Area. *Sci. Data* **2019**, *6*, 80. [CrossRef] [PubMed]
4. Albini, P. The True Case of the 1276 Fake Earthquake. *Seismol. Res. Lett.* **2011**, *82*, 111–114. [CrossRef]
5. Alfonsi, L.; Cinti, F.R.; Ventura, G. The Kinematics of the 1033 A.D. Earthquake Revealed by the Damage at Hisham Palace (Jordan Valley, Dead Sea Transform Zone). *Seismol. Res. Lett.* **2013**, *84*, 997–1003. [CrossRef]
6. Ambraseys, N.N. The Earthquake of 1 January 1837 in Southern Lebanon and N Orthern Israel. *Ann. Geophys.* **1997**, *40*, 923–935. [CrossRef]
7. Ambraseys, N.N.; Barazangi, M. The 1759 Earthquake in the Bekaa Valley: Implications for Earthquake Hazard Assessment in the Eastern Mediterranean Region. *J. Geophys. Res. Solid Earth* **1989**, *94*, 4007–4013. [CrossRef]
8. Grigoratos, I.; Poggi, V.; Danciu, L.; Rojo, G. An Updated Parametric Catalog of Historical Earthquakes around the Dead Sea Transform Fault Zone. *J. Seismol.* **2020**, *24*, 803–832. [CrossRef]
9. Zohar, M.; Salamon, A.; Rubin, R. Reappraised List of Historical Earthquakes That Affected Israel and Its Close Surroundings. *J. Seismol.* **2016**, *20*, 971–985. [CrossRef]
10. Hough, S.E.; Martin, S.S. Which Earthquake Accounts Matter? *Seismol. Res. Lett.* **2021**, *92*, 1069–1084. [CrossRef]
11. Guidoboni, E.; Ebel, J.E. *Earthquakes and Tsunamis in the Past: A Guide to Techniques in Historical Seismology*; Cambridge University Press: Cambridge, UK, 2009.
12. Hough, S.E.; Bilham, R.G. *After the Earth Quakes: Elastic Rebound on an Urban Planet*; Oxford University Press: Oxford, UK, 2005.
13. Guidoboni, E.; Stucchi, M. The Contribution of Historical Records of Earthquakes to the Evaluation of Seismic Hazard. *Ann. Geophys.* **1993**, *36*, 201–215. [CrossRef]
14. Cecić, I.; Musson, R. Macroseismic Surveys in Theory and Practice. *Nat. Hazards* **2004**, *31*, 39–61. [CrossRef]
15. Ambraseys, N. Magnitude Assessment of Northwestern European Earthquakes. *Earthq. Eng. Struct. Dyn.* **1985**, *13*, 307–320. [CrossRef]
16. Erdik, M. Earthquake Risk Assessment. *Bull. Earthq. Eng.* **2017**, *15*, 5055–5092. [CrossRef]
17. Lamata Martínez, I.; Williams, M.S.; Dyke, S.; Krötzsch, M.; Pegon, P. Next Directions in Experimental Data for Seismic Hazard Mitigation. *Eng. Struct.* **2017**, *136*, 535–546. [CrossRef]
18. Ansari, A.; El-Hussain, I.; Deif, A.; Mohamed, A.M.E.; Al-Shijbi, Y.; Al-Jabri, K.; Mandhaniya, P.; Lee, J.-H.; Alluqmani, A.E.; Mutaz, E.; et al. Integrated GIS-AHP Based Assessment of Earthquake Vulnerability and Risk for Urban Residential Buildings in Muscat, Sultanate of Oman. *Sci. Rep.* **2025**, *15*, 31995. [CrossRef] [PubMed]
19. Rovida, A.; Locati, M.; Antonucci, A.; Camassi, R. The Italian Archive of Historical Earthquake Data, ASMI. *Earth Syst. Sci. Data* **2025**, *17*, 3109–3124. [CrossRef]
20. Geller, R.J. Earthquake Prediction: A Critical Review. *Geophys. J. Int.* **1997**, *131*, 425–450. [CrossRef]
21. Gasperini, P.; Vannucci, G.; Tripone, D.; Boschi, E. The Location and Sizing of Historical Earthquakes Using the Attenuation of Macroseismic Intensity with Distance. *Bull. Seismol. Soc. Am.* **2010**, *100*, 2035–2066. [CrossRef]
22. Bakun, W.H.; Wentworth, C.M. Estimating Earthquake Location and Magnitude from Seismic Intensity Data. *Bull. Seismol. Soc. Am.* **1997**, *87*, 1502–1521. [CrossRef]

23. Sirovich, L.; Pettenati, F.; Cavallini, F. Intensity-Based Source Inversion of the Destructive Earthquake of 1694 in the Southern Apennines, Italy. *J. Geophys. Res. Solid Earth* **2013**, *118*, 6241–6257. [CrossRef]
24. Abma, R.; Kabir, N. Comparisons of Interpolation Methods. *Lead. Edge* **2005**, *24*, 984–989. [CrossRef]
25. Barbano, M.S.; Cosentino, M.; Lombardo, G.; Patané, G. *Isoseismal Maps of Calabria and Sicily Earthquakes (Southern Italy)*; University of Catania: Catania, Italy, 1980.
26. Bergamo, P.; Fäh, D.; Panzera, F.; Cauzzi, C.; Glueer, F.; Perron, V.; Wiemer, S. A Site Amplification Model for Switzerland Based on Site-Condition Indicators and Incorporating Local Response as Measured at Seismic Stations. *Bull. Earthq. Eng.* **2023**, *21*, 5831–5865. [CrossRef]
27. De Rubeis, V.; Tosi, P.; Gasparini, C.; Solipaca, A. Application of Kriging Technique to Seismic Intensity Data. *Bull. Seismol. Soc. Am.* **2005**, *95*, 540–548. [CrossRef]
28. Kang, D.; Chen, W.; Jia, Y. Bayesian Maximum Entropy Interpolation Analysis for Rapid Assessment of Seismic Intensity Using Station and Ground Motion Prediction Equations. *Front. Earth Sci.* **2024**, *12*, 1394937. [CrossRef]
29. Zohar, M. Temporal and Spatial Patterns of Seismic Activity Associated with the Dead Sea Transform (DST) during the Past 3000 Yr. *Seismol. Res. Lett.* **2019**, *91*, 207–221. [CrossRef]
30. Ambraseys, N. Descriptive Catalogues of Historical Earthquakes in the Eastern Mediterranean and the Middle East; Revisited. In *Historical Seismology: Interdisciplinary Studies of Past and Recent Earthquakes*; Fréchet, J., Meghraoui, M., Stucchi, M., Eds.; Springer: Dordrecht, The Netherlands, 2008; pp. 25–39.
31. Karcz, I. Implications of Some Early Jewish Sources for Estimates of Earthquake Hazardin the Holy Land. *Ann. Geophys.* **2004**, *47*, 759–792. [CrossRef]
32. Schafer, J.L. *Analysis of Incomplete Multivariate Data*; CRC Press: Boca Raton, FL, USA, 1997.
33. Chen, J.; Shao, J. Nearest Neighbor Imputation for Survey Data. *J. Off. Stat.* **2000**, *16*, 113–131.
34. Stekhoven, D.J.; Bühlmann, P. MissForest—Non-Parametric Missing Value Imputation for Mixed-Type Data. *Bioinformatics* **2012**, *28*, 112–118. [CrossRef] [PubMed]
35. Daberdaku, S.; Tavazzi, E.; Di Camillo, B. A Combined Interpolation and Weighted K-Nearest Neighbours Approach for the Imputation of Longitudinal ICU Laboratory Data. *J. Healthc. Inform. Res.* **2020**, *4*, 174–188. [CrossRef] [PubMed]
36. Baker, J.; White, N.; Mengersen, K. Missing in Space: An Evaluation of Imputation Methods for Missing Data in Spatial Analysis of Risk Factors for Type II Diabetes. *Int. J. Health Geogr.* **2014**, *13*, 47. [CrossRef] [PubMed]
37. Yang, H.; Yang, J.; Han, L.D.; Liu, X.; Pu, L.; Chin, S.; Hwang, H. A Kriging Based Spatiotemporal Approach for Traffic Volume Data Imputation. *PLoS ONE* **2018**, *13*, e0195957. [CrossRef] [PubMed]
38. Avni, R. The 1927 Jericho Earthquake, Comprehensive Macroseismic Analysis Based on Contemporary Sources. Ph.D. Thesis, Ben-Gurion University, Beer-Sheva, Israel, 1999.
39. Zohar, M.; Salamon, A.; Rubin, R. Earthquake Damage History in Israel and Its Close Surrounding—Evaluation of Spatial and Temporal Patterns. *Tectonophysics* **2017**, *696–697*, 1–13. [CrossRef]
40. Wald, D.J.; Quitoriano, V.; Worden, C.B.; Hopper, M.; Dewey, J.W. USGS "Did You Feel It?" Internet-Based Macroseismic Intensity Maps. *Ann. Geophys.* **2011**, *54*, 688–707. [CrossRef]
41. U. S. Geological Survey; Earthquake Hazards Program. *Advanced National Seismic System (ANSS) Comprehensive Catalog of Earthquake Events and Products*; U.S. Geological Survey: Reston, VA, USA, 2017. [CrossRef]
42. U. S. Geological Survey M 7.2—Nippes, Haiti. Available online: https://earthquake.usgs.gov/earthquakes/eventpage/us6000f65h/executive(accessed on 25 September 2024).
43. U. S. Geological Survey M 7.7–123 Km NNW of Lucea, Jamaica. Available online: https://earthquake.usgs.gov/earthquakes/eventpage/us60007idc/executive (accessed on 27 September 2024).
44. U. S. Geological Survey M 6.1–15 Km W of Düzce, Turkey. Available online: https://earthquake.usgs.gov/earthquakes/eventpage/us7000irp8/executive (accessed on 26 September 2024).
45. U. S. Geological Survey M 6.9–21 Km SSW of Kamariótissa, Greece. Available online: https://earthquake.usgs.gov/earthquakes/eventpage/usb000r2hc/executive (accessed on 27 September 2024).
46. U. S. Geological Survey M 7.1—Ridgecrest Earthquake Sequence. Available online: https://earthquake.usgs.gov/earthquakes/eventpage/ci38457511/executive (accessed on 27 September 2024).
47. U. S. Geological Survey M 6.0—The 2014 South Napa, California Earthquake. Available online: https://earthquake.usgs.gov/earthquakes/eventpage/nc72282711/executive (accessed on 26 September 2024).
48. ESRI. Near (Analysis Tools). ArcGIS Pro Tool Reference. Available online: https://doc.esri.com/en/arcgis-pro/latest/tool-reference/analysis/near.html (accessed on 30 July 2026).
49. ESRI. Generate Near Table (Analysis Tools). ArcGIS Pro Tool Reference. Available online: https://doc.esri.com/en/arcgis-pro/latest/tool-reference/analysis/generate-near-table.html (accessed on 30 July 2026).
50. Gomez-Capera, A.A.; Santulin, M.; D'Amico, M.; D'Amico, V.; Locati, M.; Meletti, C.; Varini, E. Macroseismic Intensity Attenuation Models Calibrated in Mw for Italy. *Bull. Earthq. Eng.* **2024**, *22*, 795–843. [CrossRef]

51. Taylor, P.J. *Distance Decay in Spatial Interactions*; Geo Abstracts: Norwich, UK, 1983.
52. Tobler, W.R. A Computer Movie Simulating Urban Growth in the Detroit Region. *Econ. Geogr.* **1970**, *46*, 234–240. [CrossRef] [PubMed]
53. Oliver, M.A.; Webster, R. Kriging: A Method of Interpolation for Geographical Information Systems. *Int. J. Geogr. Inf. Syst.* **1990**, *4*, 313–332. [CrossRef]
54. Bossu, R.; Gilles, S.; Mazet-Roux, G.; Roussel, F. Citizen Seismology: How to Involve the Public in Earthquake Response. In *Comparative Emergency Management: Examining Global and Regional Responses to Disasters*; Miller, D., Rivera, J., Eds.; CRC Press: Boca Raton, FL, USA, 2011; pp. 237–260.
55. Roberts, D.R.; Bahn, V.; Ciuti, S.; Boyce, M.S.; Elith, J.; Guillera-Arroita, G.; Hauenstein, S.; Lahoz-Monfort, J.J.; Schröder, B.; Thuiller, W.; et al. Cross-Validation Strategies for Data with Temporal, Spatial, Hierarchical, or Phylogenetic Structure. *Ecography* **2017**, *40*, 913–929. [CrossRef]
56. Ploton, P.; Mortier, F.; Réjou-Méchain, M.; Barbier, N.; Picard, N.; Rossi, V.; Dormann, C.; Cornu, G.; Viennois, G.; Bayol, N.; et al. Spatial Validation Reveals Poor Predictive Performance of Large-Scale Ecological Mapping Models. *Nat. Commun.* **2020**, *11*, 4540. [CrossRef] [PubMed]
57. Meyer, H.; Pebesma, E. Machine Learning-Based Global Maps of Ecological Variables and the Challenge of Assessing Them. *Nat. Commun.* **2022**, *13*, 2208. [CrossRef] [PubMed]
58. Brenning, A. Spatial Cross-Validation and Bootstrap for the Assessment of Prediction Rules in Remote Sensing: The R Package Sperrorest. In Proceedings of the 2012 IEEE International Geoscience and Remote Sensing Symposium, Munich, Germany, 22–27 July 2012; pp. 5372–5375.
59. Wadoux, A.M.J.-C.; Heuvelink, G.B.M.; De Bruin, S.; Brus, D.J. Spatial Cross-Validation Is Not the Right Way to Evaluate Map Accuracy. *Ecol. Model.* **2021**, *457*, 109692. [CrossRef]
60. Yao, X.; Fu, B.; Lü, Y.; Sun, F.; Wang, S.; Liu, M. Comparison of Four Spatial Interpolation Methods for Estimating Soil Moisture in a Complex Terrain Catchment. *PLoS ONE* **2013**, *8*, e54660. [CrossRef] [PubMed]
61. Radočaj, D.; Jug, I.; Vukadinović, V.; Jurišić, M.; Gašparović, M. The Effect of Soil Sampling Density and Spatial Autocorrelation on Interpolation Accuracy of Chemical Soil Properties in Arable Cropland. *Agronomy* **2021**, *11*, 2430. [CrossRef]
62. Pisarenko, V.F.; Pisarenko, D.V. A Modified K-Nearest-Neighbors Method and Its Application to Estimation of Seismic Intensity. *Pure Appl. Geophys.* **2022**, *179*, 4025–4036. [CrossRef]
63. Cheng, Q. Multifractal Interpolation Method for Spatial Data with Singularities. *J. S. Afr. Inst. Min. Metall.* **2015**, *115*, 235–245. [CrossRef]
64. Zaresefat, M.; Derakhshani, R.; Griffioen, J. Empirical Bayesian Kriging, a Robust Method for Spatial Data Interpolation of a Large Groundwater Quality Dataset from the Western Netherlands. *Water* **2024**, *16*, 2581. [CrossRef]
65. Musson, R.M.W.; Grünthal, G.; Stucchi, M. The Comparison of Macroseismic Intensity Scales. *J. Seismol.* **2010**, *14*, 413–428. [CrossRef]

Disclaimer/Publisher's Note: The statements, opinions and data contained in all publications are solely those of the individual author(s) and contributor(s) and not of MDPI and/or the editor(s). MDPI and/or the editor(s) disclaim responsibility for any injury to people or property resulting from any ideas, methods, instructions or products referred to in the content.

https://doi.org/10.3390/ijgi15080355